Broadband Light Management with Thermochromic Hydrogel Microparticles for Smart Windows

As Published: 10.1016/J.JOULE.2018.10.019

Publisher: Elsevier BV

Persistent URL: https://hdl.handle.net/1721.1/135895

Version: Author's final manuscript: final author's manuscript post peer review, without publisher's formatting or copy editing

Graphical Abstract

Click here to access/download;Graphical Abstract;Graphic Abstract.tif

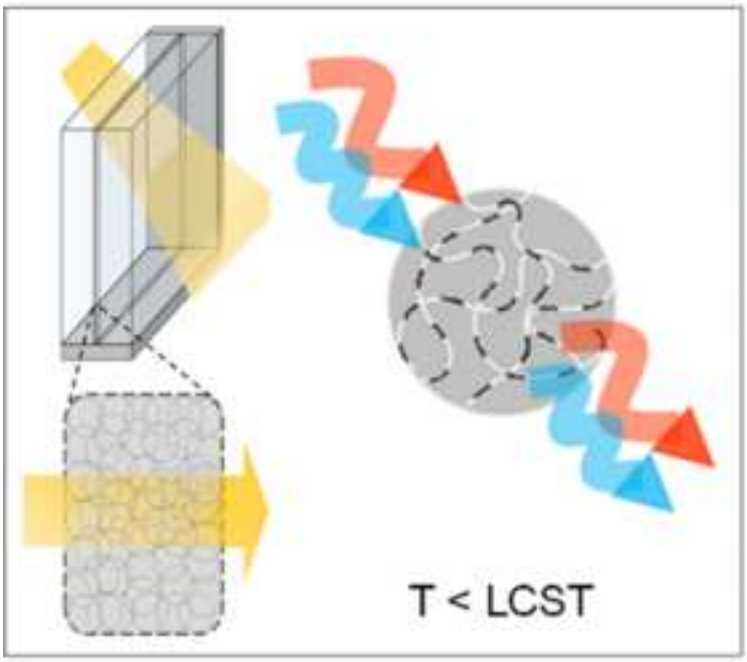

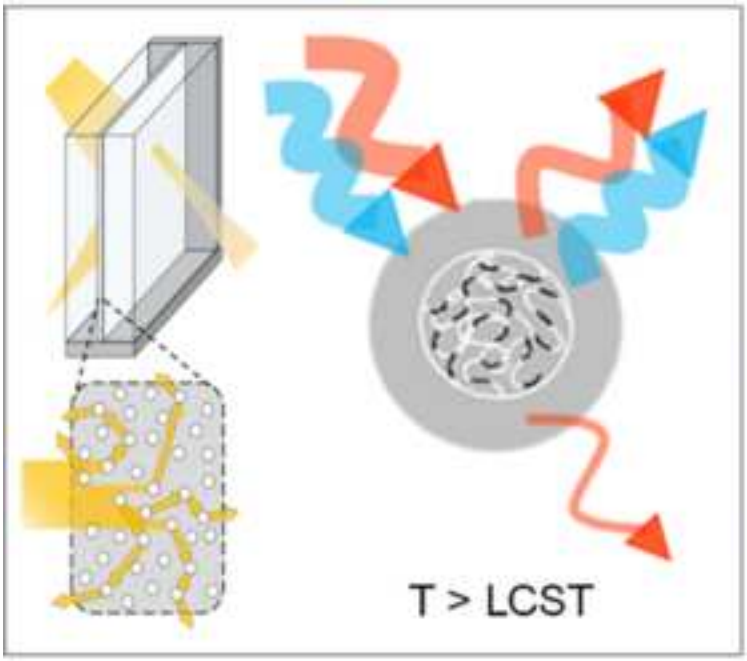

Broadband light management with thermochromic hydrogel microparticles for smart windows

Xin-Hao Li[1, 3], Chang Liu[1, 2, 3], Shien-Ping Feng[2], Nicholas Xuanlai Fang[1,4,*]

[1]Department of Mechanical Engineering, Massachusetts Institute of Technology, Cambridge, MA 02139, USA.

[2]Department of Mechanical Engineering, The University of Hong Kong, Pokfulam Rd., 999077, Hong Kong.

[3]X. Li and C. Liu contributed equally to this work

[4]Lead Contact

*Correspondence: nicfang@mit.edu

Summary

Control of solar transmission through windows promises to reduce building energy consumptions. Yet, the ability of current chromogenic technologies to regulate solar gain with the tunable extinction of phase-change materials is still far from optimum. We report a strategy for optimizing the transmittance modulation range of temperature-responsive hydrogel particles by means of tuning the light scattering behaviors through controlling particle size and internal structure. An emerging thermochromic material, poly (N-isopropylacrylamide)-2-Aminoethylmethacrylate hydrochloride (pNIPAm-AEMA) microparticles, was synthesized to demonstrate this strategy. The average size of pNIPAm-AEMA microparticles varies from 1388nm at 25˚C to 546nm at 35˚C, contributing to an unprecedented infrared transmittance modulation of 75.6%. A high luminous transmittance of 87.2% at 25˚C had also been accomplished. An investigation of the tunable scattering behaviors of pNIPAm-AEMA particles provided the mechanistic insight into light management by this class of materials, the application field of which is beyond energy-saving smart windows.

Introduction

Considerable endeavors have been devoted to light management for energy-efficient buildings to reduce energy use in heating, ventilation and air conditioning (HVAC) systems, which account for 13% in 2006 and 10% in 2020 (projected) of the total energy consumption in the US.[1] Light management using advanced smart window technologies is promising as it can theoretically lead to annual energy savings of more than 1.055×10^{15} kJ in the US (i.e., 1% of annual total energy consumption).[2] Previous transmittance modulation processes mainly rely on the change of extinction in thermochromic metal oxides or electrochromic active materials.[3] However, this reliance leads to challenges for concurrently achieving a large tuning contrast of refractive index, a broad modulation spectrum and a near room-temperature transition. In practical terms, we also need to address several critical claims for large-scale adoption in building technologies, such as luminous transparency, transmittance modulation efficiency, economics of manufacturing and operation, stability and scalability.[3,4]

Electrochromic devices achieve the dynamic modulation of transmittance over visible and infrared (IR) regions based on an electrochemical-cell structure. An operation power is usually required for electrochromic devices, such as in the majority of commercial electrochromic smart windows employing transition metal oxides (e.g., WO_3) as the active material, which switches between oxidized/reduced states during faradic charge injection/extraction,[4] and some emerging electrochromic technologies based on reversible metal electrodeposition and plasmonic nanocrystals.[5,6] In general, the fabrication of these functional thin films relies on costly physical vapor deposition and high-temperature process.[4] Up to now, cost of production and durability concerns limit the scalability of electrochromic devices.[3-5] Alternatively, thermochromic devices are considered as autonomous systems with no net energy input because the facade change can be triggered by the temperature change of the environment.[7] The simplicity of the single-component structure holds promise for industrial production and ease of implementation.

Conventional thermochromic devices are generally based on the extinction of IR light by the phase change medium that can be characterized by a change to the imaginary part of refractive index. For example, vanadium dioxide (VO_2) varies from an IR transparent state to an

IR reflective metallic state at the critical temperature (T_c) ~68°C.[7] However, such mechanism of transmittance modulation has two intrinsic limitations: 1), a transparent heating unit is needed for VO_2 to be functionalized as a smart window coating, and the resulting elevated temperature of the window surface would diminish the heat-shielding ability. Some of the best-performing VO_2 devices in literature work at 90˚C,[1,8,9] showing a solar transmittance modulation (ΔT_{solar}) of 22.3% with a luminous transmittance (T_{lum}) of 45.6% before phase transition.[8] Although dopants such as tungsten,[10] niobium,[11] and magnesium[12] have been used to reduce T_c, the introduction of foreign ions will induce degradations in ΔT_{solar} and T_{lum}.[13-15] 2) the strong inner-band and inter-band absorption of VO_2 lies in the visible region, leading to the reduced T_{lum}. Strategies like elemental doping,[15,16] antireflection coating,[17,18] porosity tuning,[19,20] and multilayered structure could improve the T_{lum} of VO_2 thin films to maximal 67.5% while the ΔT_{solar} was limited to 5.4%.[13] Furthermore, doping and microscopic structure fabrications noticeably increase the complexity and cost of manufacturing. Current techniques to conquer the preceding obstacles in conventional thermochromic windows are still far from optimum.

In this work, we focus our study on a new group of thermochromic materials that achieve light management via tunable scattering behaviors. The light blocking mechanism is elucidated with Mie scattering theory, which predicts efficient scattering in a broad solar spectrum with the aid of co-polymerized hydrogel microparticles of prescribed diameters. In particular, our aim is to achieve efficient transmittance modulation in the IR region (780 – 2500nm) where the thermal radiation contributes 53% in the total solar energy (ultraviolet 3%; visible 44%).[34] As example, we fabricated poly (N-isopropylacrylamide) (pNIPAm) and 2-Aminoethylmethacrylate hydrochloride (AEMA) co-polymerized pNIPAm-AEMA hydrogel microparticles, whose cross-link uniformity and particle size are manipulated experimentally to attain ultra-high performance in both ΔT_{solar} and T_{lum} as compared with other thermochromic counterparts (Figure 1).[9,12,21-24,26,28-33,35,36] Besides, pNIPAm-AEMA hydrogel microparticles can undergo phase transition under solar irradiance due to the low critical solution temperature (LCST) at ~32˚C, making them preferable for smart windows.[28] In contrast, an outdoor temperature higher than 50˚C is required for the phase transition of VO_2 under natural convection, which is practically infeasible. Notably, heating-cooling cycles demonstrate the excellent stability of the

device. Furthermore, the solution-phase synthesis described herein permits an industrial-scale and cost-effective production, where a 12" × 12" window device is fabricated to display its scalability and the prospect of practical applications (Figure 2 and see Figure S1).

Results and Discussion

The synthesis of co-polymerized pNIPAm-AEMA microparticles

The uniqueness of temperature-responsive pNIPAm hydrogel for light management is that their scattering behaviors can be tuned profoundly regarding to the particle size, internal structure and volume fraction of water. A homogeneously low mismatch of refractive index between pNIPAm hydrogel particles and water at the "OFF" state is responsible for high T_{lum} (Figure 3A), while the strong optical contrast between pNIPAm hydrogel particles and water is established when the polymer collapses above LCST.[37] The light is scattered at the interface between the dense polymer and surrounding water, regarding the "ON" state. An effective light management for solar heat shielding purpose requires that the light scattering covers the full solar spectrum, especially the IR region (53% of total solar energy). Problematically, heterogeneous internal structure of pNIPAm particles made by classical one-pot synthesis results in high turbidity of the hydrogel at "OFF" state (Figure $3B_1$).[38] Meanwhile, pNIPAm particles synthesized by radical emulsion polymerization reach the size limitation that the size parameter ($2\pi r/\lambda$) comparable to 1 only in the visible region,[38-40] leading to inefficient scattering in the IR region at "ON" state (Figure $3B_2$). In order to extend the transmittance modulation spectrum and guarantee the high T_{lum}, the synthesis strategy is to enlarge the hydrogel particle size and maintain a homogeneous cross-link density.

The aforementioned requirements on the scattering behaviors of hydrogel particles were achieved by co-polymerizing pNIPAm and AEMA via a continuous feeding solution-phase synthesis (Figure $3B_3$). The AEMA co-polymer modified the surface charge of particles with the positive terminal primary amine groups.[41] The electrostatic repulsion of the hydrogel particles was diminished, which can be corroborated by the change of the zeta potential from −23.9mV to −9.0mV. Thus, the oligomers precipitated on primary particles and consequently to increase

the particle size. The D_h enlarges to 1388nm at 25˚C and 546nm at 35˚C (Figure 3C), contributing to a size parameter ($2\pi r/\lambda$) comparable to 1 in the IR region. Meanwhile, the continuous feeding method kept a constant monomer concentration and a reaction rate throughout the entire synthesis. The hydrogel particles were formed with a homogeneous internal structure, contributing to a very low scattering contrast to surrounding water at the swollen state. The temperature response of the pNIPAm-AEMA microparticles was evaluated by differential scanning calorimetry (DSC), revealing the endothermic peak temperature of 31.6˚C and the exothermic peak temperature of 30.9˚C (see Figure S2). Additionally, the strong phase transition from swollen to de-swollen state was observed by optical microscopy (see Figure S3A and B). In contrast, the average hydrodynamic diameter (D_h) of pure pNIPAm particles is 548nm at 25˚C and shrinks to 282nm at 35˚C (Figure 3C), which reaches its size limitation in spite of carrying out the polymerization in a longer period of time and with a larger amount of monomer (see Figure S4). Our synthesis achieves the homogeneous cross-link density of particle and the controlled particle size from 200 to 2000nm (Figure S3C), which simultaneously fulfills the high T_{lum} and the extending transmittance modulation in IR region for the first time. Besides, compared with the thin-film manufacture of thermochromic VO_2, such a solution-phase synthesis of hydrogel particles suggests great potential for industrial-scale and cost-effective production.

Scattering behavior of pNIPAm-AEMA microparticles

Tunable scattering behaviors of pNIPAm-AEMA microparticles herein are elaborated in terms of the change of particle size parameter and optical density. Particularly, the scattering cross-section and refractive index were investigated based on Mie theory and Beer-Lambert law,[42,43] which exhibits that the effective modulation of IR light by scattering could be delivered in response to the size parameter around 1 in the IR wavelength region and a strong enhancement of real part of refractive index above the LCST. Figure $3D_1$ and $3D_2$ show the complex refractive index of pNIPAm-AEMA microparticles, which was deduced from the attenuation coefficient (μ_t) of the diluted suspension (see Figure S5). The n of particles closes to the n of water at the swollen state, which is attributed to the large volume fraction of water and a homogeneous cross-linked structure. The small scattering cross-section (σ_s) before phase transition is beneficial for a high T_{lum} (Figure $3D_3$). Meanwhile, the small absorbing cross-section (σ_a) indicates a low absorption

loss in the pNIPAm-AEMA (Figure 3D$_4$), where two peaks near 1450nm and 1930nm are associated with the absorption of water molecules (see Figure S5). After the phase transition, the internal structure of pNIPAm-AEMA microparticles changes from a homogeneous water-rich state to the collapsed state. The *n* approaches that of the bulk polymer with the reduction in the volume fraction of water. The *n* of pNIPAm-AEMA at the de-swollen state increases to approximately 1.45 in the visible region and to 1.40 in the IR region, which is in good accordance with the *n* of hydrogel particles with similar chemical structures estimated by the effective medium approximation.[42,43] Figure 3D$_3$ depicts that the σ_s of pNIPAm-AEMA appreciably increases in both the visible and IR regions after the phase transition. In contrast, the σ_s of pure pNIPAm particles in the IR region is 2 orders lower due to the size limitation (see Figure S6 and S7), which narrows the transmittance modulation region. The dependence of σ_s on different particle sizes is also investigated (Figure 3D$_3$), indicating that the enlargement of particle size is responsible for delivering a stronger scattering in the broad solar spectrum. On the other hand, the σ_a of pNIPAm-AEMA microparticles keeps a similar value (Figure 3D$_4$), indicating that the transmittance is modulated via the enhancement of scattering, with respect to the increases in the real part of the refractive index, instead of absorbing.

Transmittance modulation by pNIPAm-AEMA hydrogel devices

To fulfill efficient light management for energy saving purposes, the ideal thermochromic smart window requires a near room-temperature transition and a sharp gradient of transmittance.[44] The transmittance spectra of pNIPAm-AEMA hydrogel device (250 – 2500nm) at the layer thickness of 240μm is reported in Figure 4A. At temperatures below LCST (22˚C or 25˚C), the T_{lum}, T_{IR} and T_{solar} are as high as 87.2%, 81.6% and 84.1%, respectively (Figure 4B). Figure 4B shows luminous (ΔT_{lum}), IR (ΔT_{IR}) and solar (ΔT_{solar}) transmittance modulations at different temperatures. The phase transition started at 31°C along with a ΔT_{solar} of 26.2%, implying the strong temperature-responsive nature of pNIPAm-AEMA microparticles. Notably, at 34˚C, the T_{IR} was significantly reduced from 81.6% to 6.0%, indicating an unprecedented high ΔT_{IR} of 75.6%. As a result, the ΔT_{solar} was boosted to 81.3%. Such a dramatic transition is desired for promptly blocking a large amount of solar irradiance.[44] In contrast, pure pNIPAm particles with the small size (D_h = 548nm at 25˚C and 282nm at 35˚C) barely afforded transmittance modulation

in the IR region (see Figure S8). The pNIPAm hydrogel layer with the same thickness (240μm) only showed a low ΔT_{IR} of 32.1%, leading to a limited ΔT_{solar} of 59.1% (see Figure S8). Although a hybrid of hydrogel with VO_2 or antimony-tin oxide nanoparticles has been attempted to improve ΔT_{IR},[29,35] the operating temperature of metal oxide nanoparticle/hydrogel composite is as high as 80˚C. Also, the complicated fabrication procedures for both nanoparticle doping and composite preparation cause difficulties for practical application. Furthermore, the performance of the pNIPAm-AEMA hydrogel device regarding transmittance modulations is superior to all known VO_2-based thermochromic materials and thermochromic films made by hydrogels, hydrogel/VO_2 composites, ionogels, and LETCs.[9,12,21-24,26,28-33,35,36]

The excellent light blocking by pNIPAm-AEMA hydrogel device in the IR spectrum results from microparticles whose dimensionless size parameter ($2\pi r/\lambda$) reaches unity in the IR region. The IR light is effectively scattered by microparticles in the device with the layer thickness from thin (40μm) to thick (380μm) (Figure S9A). To the contrary, the transmittance modulation of pNIPAm particles is confined in the visible spectrum and is hardly improved by increasing the layer thickness (see Figure S9B). A Monte-Carlo simulation of multiple scattering process based on Mie theory was applied to investigate the dependence of ΔT_{solar} on the layer thickness.[45] The experiment results of transmittance modulation at different layer thicknesses were well reproduced, in which the estimated *n* and *k* of hydrogel particles were adopted (see Supplemental Note 1, Figure S9, S10). Owing to the broadband transmittance modulation, ΔT_{solar} of pNIPAm-AEMA hydrogel is higher than ΔT_{solar} of pNIPAm hydrogel for any given layer thickness (see Figure S11A). Meanwhile, the simulation shows the potential of pNIPAm-AEMA hydrogel of achieving a high T_{lum} and maintaining a decent ΔT_{solar} after phase transition by further reducing the layer thickness (see Figure S11B).

Solar-energy shielding and device stability

Practical applications of smart windows raise the claims of reducing the solar gain and maintaining stability. A direct solar-energy modulation (DSEM) was introduced to characterize the reduction of the heat flux from solar irradiance due to the phase transition of the window device (see Supplemental Note 2). The irradiance from a solar simulator was slashed by 69.5% after passing through a pNIPAm-AEMA device, which is significantly higher than all existing

smart window products on the market (see Figure S12).[46] The pNIPAm-AEMA device was also installed on a chamber, and the temperature change inside the chamber was recorded under 1 sun, air mass 1.5 illumination (Figure 5A). The window made by double glass slides was used as a control experiment, where the initial temperature of 25.0˚C rapidly increased to 39.1˚C after 20min and reached a plateau at 30min (14.1˚C increments). Whereas the phase transition of the pNIPAm-AEMA device was spontaneously triggered and completed after 5min illumination and the inner temperature only increased by 9.2˚C at 30min. Notably, the inner chamber temperature raised merely 1.3˚C once the phase transition of the pNIPAm-AEMA hydrogel was completed. A slight decline in temperature after the phase transition indicates a net negative heat gain inside the chamber induced by a sudden opacity change where the heat dissipation was more significant than the heat input from illumination. After 10min illumination, the outside temperature reached 40.9˚C, and the inside temperature increased gradually due to heat conduction and convection. A smaller temperature rising rate of 0.10˚C/min was delivered, compared with the rising rate of 0.26˚C/min in the control experiment.

Figure 5B_1 demonstrates visible transparency of the pNIPAm-AEMA device before and after phase transition, and Figure 5B_2 shows the corresponding thermal infrared images. The pNIPAm-AEMA device became opaque when the temperature raised to 35˚C. Especially, the outstanding IR modulation of pNIPAm-AEMA device was proved by the IR images (Figure 5B_3). At 25˚C, the NIR light (850 – 2200nm) passed through an "MIT" logo and was captured by IR camera, whose intensity was significantly slashed once the phase transition was triggered, indicating an excellent ΔT_{IR}, which is barely obtained by VO_2 thin films and other kinds of thermochromic thin films.[1,9,28,31]

A heating-cooling test of 1000 cycles was conducted on the pNIPAm-AEMA device to test its stability for long-term operation, which shows less than a 4% decrease of ΔT_{IR} (Figure 5C and 5D). Besides, no shrinkage of the hydrogel film was observed during heating-cooling cycles (see Figure S13, Supplementary video). Such high stability regarding the number of testing cycles has not yet been reported as most smart windows made by hydrogels suffering the severe and non-reversible deformation after cyclic tests.[28,31] Additionally, the pNIPAm-AEMA device

maintained its transparency at −2.1°C, and the phase transition was reserved when the sample was heated to 32.1°C (Figure S14).

Conclusions

In summary, a new type of light management device based on thermochromic pNIPAm-AEMA microparticles has been demonstrated. The large and broadband transmittance modulation makes the device ideal for energy-saving applications. Especially, by tailoring the particle size and internal structure, the pNIPAm-AEMA hydrogel effectively extends light rejection into the IR region, contributing to a significantly enhanced ΔT_{IR} of 75.6% and an ultra-high ΔT_{solar} of 81.3%. Meanwhile, the superiorities of hydrogel over conventional VO_2-based thermochromic materials are maintained, exhibiting a high T_{lum} of 87.2% and a low phase transition temperature ~32˚C. A decline of indoor temperature ~5˚C can be expected by using the pNIPAm-AEMA thermochromic windows, whose excellent stability and scalability also display its prospect of practical applications. Building upon the advancement of light management in the use of pNIPAm-AEMA microparticles over counterpart thermochromic materials, future progress in dynamic transmittance modulation is enabled by pursuing the optimal mechanism that leads to the change in the refractive index. The tunable scattering behaviors of hydrogel particles not only pave a way to revamp energy-saving smart windows but will also be broadly applicable to optical modulators, displays, and invisibility cloaking.[47,48]

Experimental Procedures

Materials

The N-Isopropylacrylamide monomer (NIPAm, 98%), N, N′-methylenebis (acrylamide) (BIS, 99%) cross-linker, ammonium persulfate (APS, ≥98%) initiator, sodium dodecyl sulfate (SDS ,

≥ 98.5%) surfactant were purchased from Sigma-Aldrich. 2-Aminoethylmethacrylate hydrochloride monomer (AEMA, 95%) was purchased from Polyscienes.

Synthesis of pNIPAm-AEMA microparticles

The pNIPAm-AEMA particles were synthesized by the continuous feeding of NIPAm and AEMA co-monomers into the reaction vessel. 6.00g NIPAm, 0.15g BIS and 25.8mg AEMA were dissolved in 150ml DI water and purged with N_2 for 20min. The one-fifth as-prepared solution was mixed with 60ml DI water and heated to 80˚C, and 6ml of 22.8mM APS was added to initiate the polymerization. The remaining solution was continuously fed into the reaction vessel at a rate of 1ml/min, and the solution was stirred intensively during the entire polymerization. The reaction was stopped after 75min, and the colloidal suspension was quenched rapidly in a freezer. To improve the stability of colloid suspensions, 0.87mM SDS surfactant was dissolved in the colloid suspension by ultrasonication after synthesis and the temperature of the suspension was kept below 30˚C. The size of co-polymerized pNIPAm-AEMA particles was controlled by continuously feeding a constant concentration of co-monomers and predictably stopping the reaction at different feeding times (Figure S3C). The pure pNIPAm hydrogel particles were synthesized similarly (see Supplemental Note 3). The effects of applying AEMA co-monomer and SDS surfactant in synthesis were elaborated in Figure S15.

Device fabrication

The hydrogel particles suspension was centrifuged at 13,000rpm for 1.5hours (MiniSpin plus, Eppendorf, Germany). The hydrogel thin-film devices were fabricated by injecting close-packed pNIPAm-AEMA or pNIPAm hydrogel particles in between double glass slides, where the thickness of the layer was controlled by using thermoplastic sealing films (Meltonix 1170, DuPont Surlyn).

Characterization

Dynamic light scattering (DLS) measurements were performed on a Dynamic Nanostar (Wyatt Technology, USA) with a laser at the wavelength of 658nm. The hydrogel suspensions were diluted to 50ppm and injected into UV/Vis cuvettes (Eppendorf International). The diffusion

coefficient (*D*) was obtained from the measured autocorrelation function (ACF), by which the hydrodynamic diameter (D_h) of a diffusion sphere was determined via the Stokes-Einstein equation (1):[49]

$$D_h = \frac{kT}{3\pi\eta D} \tag{1}$$

where *k* is Boltzmann's constant, *T* is the absolute temperature, η is the viscosity of the solvent. The temperature was controlled by a thermostat with an accuracy of ± 0.1˚C.

Differential scanning calorimetry (DSC) analysis was conducted on Discovery DSC (TA Instruments) over the temperature between 20 to 45˚C with a heating/cooling rate of 2˚C/min under nitrogen flow. The closely packed hydrogel particles after centrifuging were applied to the DSC measurement without further treatment.

The transmittance spectra were collected using a Lambda 1050 UV-Vis-NIR spectrophotometer (PerkinElmer, USA) at normal incidence. The calculations of integral luminous transmittance T_{lum} (380 – 780nm), IR transmittance T_{IR} (780 – 2500nm), solar transmittance T_{sol} (280 – 2500nm) and corresponding transmittance modulations can be found in equation (2) and (3), respectively:[13]

$$T_{lum/IR/solar} = \frac{\int \varphi_{lum/IR/soalr}(\lambda) T(\lambda) d\lambda}{\int \varphi_{lum/IR/soalr}(\lambda) d\lambda} \tag{2}$$

$$\Delta T_{lum/IR/solar} = T_{lum/IR/solar}(@\mathrm{LT}) - T_{lum/IR/solar}(@\mathrm{HT}) \tag{3}$$

where $T(\lambda)$ denotes the recorded transmittance at a particular wavelength, φ_{lum} is the standard luminous efficiency function for the photopic vision of human eyes,[50] and $\varphi_{IR/solar}$ is the IR/solar irradiance spectrum for air mass 1.5.[34]

The solar-energy shielding test was conducted on a model chamber with a dimension of 0.15×0.10×0.08m^3, which was covered by rigid melamine insulation sheets. The 0.04×0.05m^2 window devices made by bare double glass slides or the hydrogel device with a layer thickness of 380μm were assembled upon the model chamber. The illumination intensity of a standard solar simulator (Peccell PEC-L01, Japan) was calibrated to air mass 1.5 illumination (100mWcm^{-2}) on the top side of the window. The temperatures inside and outside of the chamber were

measured by a thermometer simultaneously. The infrared thermal images were recorded via a thermal imaging camera (FLIR Systems, USA). The IR images were captured by an IR camera (IR camera 85400, FJW Optical System, USA) with the sensitivity from 400 to 1800nm. A near-infrared (NIR) bulb incorporated with a long pass filter (850 – 2200nm, Throlab FEL0850) was utilized as the irradiation light source for the demonstration of IR modulation.

Evaluation of optical properties of hydrogel particles

The scattering cross-sections of the hydrogel particles were evaluated with an inverse method based on Mie theory.[42] On the basis of Beer-Lambert law,[51] the attenuation coefficient (μ_t) of a low-concentration particle suspension could be obtained by determining the linear dependence of ln(T) on the thickness of suspension (d),[51]

$$\mu_t(\lambda) = -\frac{\Delta \ln[T(\lambda)]}{\Delta d} \tag{4}$$

The attenuation coefficient is determined by scattering and absorbing,[51]

$$\mu_t(\lambda) = \mu_s(\lambda) + \mu_a(\lambda) \tag{5}$$

$$\mu_s = c\sigma_s \tag{6}$$

$$\mu_a = c\sigma_a + \frac{4\pi k_w}{\lambda} \tag{7}$$

where μ_s and μ_a are the scattering and absorbing coefficient, respectively. Besides, σ_s and σ_a denote the scattering and absorbing cross-section, respectively. c is the concentration of particles and k_w is the imaginary refractive index of water.[52] The transmittance of 10wt% as-synthesized suspensions with the thickness from 130 to 670μm was measured to determine the attenuation coefficient. We made the assumption that the particles at swollen state are incompressible. The concentration of the hydrogel particles was estimated by measuring the volume of particles after removing the surrounding water via centrifuging and dividing by $1/6\pi D_h^3$. The scattering and absorption cross-sections of hydrogel particles were calculated based on a modified Mie scattering code.[42,53] Here the fitted refractive index was chosen to keep the continuity of the real part (n) through both the visible and IR regions and to achieve a relative error less than 1% between the fitted and measured attenuation coefficients. Stepsize of 10^{-4} in

n and 10^{-6} in the imaginary refractive index (*k*) for the visible region and 10^{-5} for the IR region were used in the fitting.

Acknowledgments

The authors acknowledge the financial support of the HKUST-MIT Consortium (Grant No. ITS/410/16FP). N.X.F, C.L., and X.H.L. acknowledge the Institute for Soldiers Nanotechnology (ISN), Biophysical Instrumentation Facility (BIF) and Center for Materials Science and Engineering (CMSE) Shared Facilities at the Massachusetts Institute of Technology (MIT). X.H.L. and C.L acknowledge Jordan Handler and Zheng Jie Tan for proofreading. C.L. acknowledges the support from the University of Hong Kong for the exchange program (Pilot Scheme) and the General Research Fund of the Research Grants Council of Hong Kong Special Administrative Region, China (Award No. 17202314 and 17204516).

Author contributions

X.H.L., C.L., and N.X.F. developed the concept, designed and conducted the experiments. S.P.F. contributed to the device preparation and solar simulator experiments. N.X.F., C.L., and X.H.L. prepared the manuscript and contributed to the interpretation of the results. X.H.L. and C.L. contribute equally to this work.

Declaration of interests

N.X.F., C.L., and X.H.L. are inventors on an invention disclosure at MIT (case no. 20597; created at 1 June 2018) related to this work. The authors declare no competing interests.

References

1 Gao, Y., Wang, S., Kang, L., Chen, Z., Du, J., Liu, X., Luo, H. and Kanehira, M. (2012) VO2-Sb:SnO2 composite thermochromic smart glass foil. Energy Environ. Sci. *5*, 8234-8237.

2 Apte, J. and Arasteh, D. (2008) Window-related energy consumption in the US residential and commercial building stock.

3 Wang, Y., Runnerstrom, E. L. and Milliron, D. J. (2016) Switchable materials for smart windows. Annu. Rev. Chem. Biomol. Eng. *7*, 283-304.

4 Runnerstrom, E. L., Llordés, A., Lounis, S. D. and Milliron, D. J. (2014) Nanostructured electrochromic smart windows: traditional materials and NIR-selective plasmonic nanocrystals. Chem. Commun. *50*, 10555-10572.

5 Barile, C. J., Slotcavage, D. J., Hou, J., Strand, M. T., Hernandez, T. S. and McGehee, M. D. (2017) Dynamic windows with neutral color, high contrast, and excellent durability using reversible metal electrodeposition. Joule *1*, 133-145.

6 Kim, J., Ong, G. K., Wang, Y., LeBlanc, G., Williams, T. E., Mattox, T. M., Helms, B. A. and Milliron, D. J. J. N. l. (2015) Nanocomposite architecture for rapid, spectrally-selective electrochromic modulation of solar transmittance. Nano Lett. *15*, 5574-5579.

7 Kamalisarvestani, M., Saidur, R., Mekhilef, S. and Javadi, F. (2013) Performance, materials and coating technologies of thermochromic thin films on smart windows. Renew. Sust. Energ. Rev. *26*, 353-364.

8 Kang, L., Gao, Y., Luo, H., Chen, Z., Du, J. and Zhang, Z. (2011) Nanoporous thermochromic VO2 films with low optical constants, enhanced luminous transmittance and thermochromic properties. ACS Appl. Mater. Inter. *3*, 135-138.

9 Chen, Z., Gao, Y., Kang, L., Cao, C., Chen, S. and Luo, H. (2014) Fine crystalline VO2 nanoparticles: synthesis, abnormal phase transition temperatures and excellent optical properties of a derived VO2 nanocomposite foil. J. Mater. Chem. A *2*, 2718-2727.

10 Zhou, Y., Ji, S., Li, Y., Gao, Y., Luo, H. and Jin, P. (2014) Microemulsion-based synthesis of V1−xWxO2@SiO2 core–shell structures for smart window applications. J. Mater. Chem. C *2*, 3812-3819.

11 Piccirillo, C., Binions, R. and Parkin, I. P. (2007) Nb-doped VO2 thin films prepared by aerosol-assisted chemical vapour deposition. Eur. J. Inorg. Chem. *2007*, 4050-4055.

12 Zhou, J., Gao, Y., Liu, X., Chen, Z., Dai, L., Cao, C., Luo, H., Kanahira, M., Sun, C. and Yan, L. (2013) Mg-doped VO2 nanoparticles: hydrothermal synthesis, enhanced visible transmittance and decreased metal–insulator transition temperature. Phys. Chem. Chem. Phys. *15*, 7505-7511.

13 Cui, Y., Ke, Y., Liu, C., Chen, Z., Wang, N., Zhang, L., Zhou, Y., Wang, S., Gao, Y. and Long, Y. (2018) Thermochromic VO2 for energy-efficient smart windows. Joule.

14 Manning, T. D., Parkin, I. P., Blackman, C. and Qureshi, U. (2005) APCVD of thermochromic vanadium dioxide thin films—solid solutions V2−xMxO2 (M= Mo, Nb) or composites VO2: SnO2. J. Mater. Chem. *15*, 4560-4566.

15 Dai, L., Chen, S., Liu, J., Gao, Y., Zhou, J., Chen, Z., Cao, C., Luo, H. and Kanehira, M. (2013) F-doped VO2 nanoparticles for thermochromic energy-saving foils with modified color and enhanced solar-heat shielding ability. Phys. Chem. Chem. Phys. *15*, 11723-11729.

16 Chen, S., Dai, L., Liu, J., Gao, Y., Liu, X., Chen, Z., Zhou, J., Cao, C., Han, P. and Luo, H. (2013) The visible transmittance and solar modulation ability of VO 2 flexible foils simultaneously improved by Ti doping: an optimization and first principle study. Phys. Chem. Chem. Phys. *15*, 17537-17543.

17 Zhang, Z., Gao, Y., Luo, H., Kang, L., Chen, Z., Du, J., Kanehira, M., Zhang, Y. and Wang, Z. L. (2011) Solution-based fabrication of vanadium dioxide on F: SnO2 substrates with largely enhanced thermochromism and low-emissivity for energy-saving applications. Energy Environ. Sci. *4*, 4290-4297.

18 Koo, H., Shin, D., Bae, S.-H., Ko, K.-E., Chang, S.-H. and Park, C. (2014) The effect of CeO 2 antireflection layer on the optical properties of thermochromic VO2 film for smart window system. J. Mater. Eng. Perform. *23*, 402-407.

19 Cao, X., Wang, N., Law, J. Y., Loo, S. C. J., Magdassi, S. and Long, Y. (2014) Nanoporous thermochromic VO2 (M) thin films: controlled porosity, largely enhanced luminous transmittance and solar modulating ability. Langmuir *30*, 1710-1715.

20 Ding, S., Liu, Z., Li, D., Zhao, W., Wang, Y., Wan, D. and Huang, F. (2013) Tunable assembly of vanadium dioxide nanoparticles to create porous film for energy-saving applications. ACS Appl. Mater. Inter. *5*, 1630-1635.

21 Mlyuka, N., Niklasson, G. A. and Granqvist, C.-G. (2009) Thermochromic multilayer films of VO2 and TiO2 with enhanced transmittance. Sol. Energ. Mat. Sol. C. *93*, 1685-1687.

22 Chen, Z., Gao, Y., Kang, L., Du, J., Zhang, Z., Luo, H., Miao, H. and Tan, G. (2011) VO2-based double-layered films for smart windows: optical design, all-solution preparation and improved properties. Sol. Energ. Mat. Sol. C. *95*, 2677-2684.

23 Zhu, J., Huang, A., Ma, H., Chen, Y., Zhang, S., Ji, S., Bao, S. and Jin, P. (2017) Hybrid films of VO2 nanoparticles and a nickel (ii)-based ligand exchange thermochromic system: excellent optical performance with a temperature responsive colour change. New J. Chem. *41*, 830-835.

24 Mlyuka, N. R., Niklasson, G. A. and Granqvist, C. G. (2009) Thermochromic VO2-based multilayer films with enhanced luminous transmittance and solar modulation. Phys. Status Solidi A *206*, 2155-2160.

25 Liu, C., Wang, S., Zhou, Y., Yang, H., Lu, Q., Mandler, D., Magdassi, S., Tay, C. Y. and Long, Y. (2018) Index-tunable anti-reflection coatings: Maximizing solar modulation ability for vanadium dioxide-based smart thermochromic glazing. J. Alloy. Compd. *731*, 1197-1207.

26 Shen, N., Chen, S., Chen, Z., Liu, X., Cao, C., Dong, B., Luo, H., Liu, J. and Gao, Y. (2014) The synthesis and performance of Zr-doped and W–Zr-codoped VO2 nanoparticles and derived flexible foils. J. Mater. Chem. A *2*, 15087-15093.

27 Zhu, J., Huang, A., Ma, H., Ma, Y., Tong, K., Ji, S., Bao, S., Cao, X. and Jin, P. (2016) Composite film of vanadium dioxide nanoparticles and ionic liquid–nickel–chlorine complexes with excellent visible thermochromic performance. ACS Appl. Mater. Inter. *8*, 29742-29748.

28 Zhou, Y., Cai, Y., Hu, X. and Long, Y. (2014) Temperature-responsive hydrogel with ultra-large solar modulation and high luminous transmission for "smart window" applications. J. Mater. Chem. A *2*, 13550-13555.

29 Zhou, Y., Cai, Y., Hu, X. and Long, Y. (2015) VO2/hydrogel hybrid nanothermochromic material with ultra-high solar modulation and luminous transmission. J. Mater. Chem. A *3*, 1121-1126.

30 Zhou, Y., Layani, M., Wang, S., Hu, P., Ke, Y., Magdassi, S. and Long, Y. (2018) Fully printed flexible smart hybrid hydrogels. Adv. Funct. Mater. *28*, 1705365.

31 Lee, H. Y., Cai, Y., Velioglu, S., Mu, C., Chang, C. J., Chen, Y. L., Song, Y., Chew, J. W. and Hu, X. M. (2017) Thermochromic ionogel: a new class of stimuli responsive materials with super cyclic stability for solar modulation. Chem. Mater. *29*, 6947-6955.

32 Wang, S., Xu, Z., Wang, T., Xiao, T., Hu, X.-Y., Shen, Y.-Z. and Wang, L. (2018) Warm/cool-tone switchable thermochromic material for smart windows by orthogonally integrating properties of pillar [6] arene and ferrocene. Nat. Commun. *9*.

33 Harlan J. B., Paul H. O. Jr., Douglas A. V. G., Brad S. V., and Derick D. W. (2006) Ligand exchange thermochromic, (LETC), systems. US Pat. US 841045 B2.

34 Standard, A. (2007) G173,"Standard tables for reference solar spectral irradiances: direct normal and hemispherical on 37 tilted surface," Amer. Society for Testing Matls., West Conshocken PA, USA.

35 Lee, H. Y., Cai, Y., Bi, S., Liang, Y. N., Song, Y. and Hu, X. M. (2017) A dual-responsive nanocomposite toward climate-adaptable solar modulation for energy-saving smart windows. ACS Appl. Mater. Inter. *9*, 6054-6063.

36 Chen, Z., Cao, C., Chen, S., Luo, H. and Gao, Y. (2014) Crystallised mesoporous TiO2 (A)–VO2 (M/R) nanocomposite films with self-cleaning and excellent thermochromic properties. J. Mater. Chem. A *2*, 11874-11884.

37 Schild, H. G. (1992) Poly(N-isopropylacrylamide): experiment, theory and application. Prog. Polym. Sci. *17*, 163-249.

38 Acciaro, R., Gilányi, T. and Varga, I. (2011) Preparation of monodisperse poly (N-isopropylacrylamide) microgel particles with homogenous cross-link density distribution. Langmuir *27*, 7917-7925.

39 Gao, J. and Hu, Z. (2002) Optical properties of N-isopropylacrylamide microgel spheres in water. Langmuir *18*, 1360-1367.

40 Fernandez-Nieves, A., Wyss, H., Mattsson, J. and Weitz, D. A. (2011). Microgel suspensions: fundamentals and applications. (John Wiley & Sons, Inc.)

41 Still, T., Chen, K., Alsayed, A. M., Aptowicz, K. B. and Yodh, A. (2013) Synthesis of micrometer-size poly (N-isopropylacrylamide) microgel particles with homogeneous crosslinker density and diameter control. J. Colloid Interf. Sci *405*, 96-102.

42 Fu, Q. and Sun, W. (2001) Mie theory for light scattering by a spherical particle in an absorbing medium. Appl. Optics. *40*, 1354-1361.

43 Beer, A. (1852) Bestimmung der absorption des rothen lichts in farbigen flussigkeiten. Ann. Physik *162*, 78-88.

44 Warwick, M. E., Ridley, I. and Binions, R. (2014) The effect of transition gradient in thermochromic glazing systems. Energ. Buildings. *77*, 80-90.

45 Ramella-Roman, J. C., Prahl, S. A. and Jacques, S. L. (2005) Three Monte Carlo programs of polarized light transport into scattering media: part I. Opt. Express *13*, 4420-4438.

46 Lawrence Berkeley National Laboratory, International Glazing Database, version 60 https://windows.lbl.gov/software/igdb. (accessed June 2018).

47 Schittny, R., Kadic, M., Bückmann, T. and Wegener, M. (2014) Invisibility cloaking in a diffusive light scattering medium. Science, 1254524.

48 Hsu, C. W., Zhen, B., Qiu, W., Shapira, O., DeLacy, B. G., Joannopoulos, J. D. and Soljačić, M. (2014) Transparent displays enabled by resonant nanoparticle scattering. Nat. Commun. *5*, 3152.

49 Teraoka, I. (2002). Polymer solutions: an introduction to physical properties. (John Wiley & Sons, Inc.)

50 Wyszecki, G. and Stiles, W. S. (1982). Color science. Vol. 8 (Wiley New York).

51 Beer. (1852) Bestimmung der Absorption des rothen Lichts in farbigen Flüssigkeiten. Annalen der Physik *162*, 78-88.

52 Palmer, K. F. and Williams, D. (1974) Optical properties of water in the near infrared. JOSA *64*, 1107-1110.

53 Mätzler, C. (2002) MATLAB functions for Mie scattering and absorption, version 2. IAP Res. Rep. *8*, 1-24.

Figure 1 Thermochromic performance (solar transmittance modulation, ΔT_{solar}, after phase transition, and luminous transmittance, T_{lum}, before phase transition) in some of the best reported films: single-layered VO_2 films,[21-23] multi-layered VO_2 films,[21,22,24,25] doped VO_2 films,[10,12,15,26] nanoporous VO_2 films,[8] VO_2 composite films,[1,27] VO_2/nickel (II)-based ligand exchange hybrid (NLET) films,[23] hydrogel films,[28] hydrogel/VO_2 composite films,[29] Si/Al hydrogel hybrid films,[30] ionogel films,[31] ferrocene modified ethylene glycol-modified pillar[6]arene (Fc-gel·EGP6),[32] ligand exchange of thermochromic films (LETC),[33] and the pNIPAm-AEMA films. Hollow and half-hollow symbols indicate the ΔT_{solar} of thermochromic films at phase transition temperature from 60˚C to 100˚C. Solid symbols indicate the thermochromic films with low phase transition temperature (≤ 40˚C). In particular, the ΔT_{solar} of hydrogels, ionogels, LETC, and Fc-gel·EGP6 are acquired at the phase transition temperature of 40˚C, while, the ΔT_{solar} of the pNIPAm-AEMA films are obtained at 34˚C in this work.

Figure 2 Images of a 12" ×12" pNIPAm-AEMA device. (A) Image the pNIPAm-AEMA device at an ambient temperature of 5˚C. (B) The phase transition of a "palm-print" area in the pNIPAm-AEMA device was triggered by the hand.

Figure 3 Temperature-responsive pNIPAm-AEMA microparticles. (A) Schematic of transmittance modulation based on the tunable scattering behaviors of hydrogel particles. Light manipulating with the aid of the phase transition of (B_1) pNIPAm particles produced by one-pot synthesis; (B_2) pNIPAm particles synthesized by continuous feeding method; (B_3) pNIPAm-AEMA co-polymerized microparticles. Visible light and IR light are presented by blue and red arrows, respectively. (C) Hydrodynamic diameters of pNIPAm-AEMA microparticles (red solid) and pNIPAm particles (green dashed) at different temperatures. (D_1 and D_2) Real (*n*) and imaginary (*k*) refractive index of the pNIPAm-AEMA microparticles at 25°C and 35°C, respectively. The dashed line in D_1 shows the *n* of water. (D_3 and D_4) corresponding scattering and absorbing cross-sections of the pNIPAm-AEMA microparticles at 25°C and 35°C, respectively. Estimated scattering cross-sections of pNIPAm-AEMA with a diameter of 400nm, 800nm and 1000nm at the de-swollen state are illustrated as solid curves.

Figure 4 Characterization of the pNIPAm-AEMA hydrogel film. (A) Transmittance spectra of pNIPAm-AEMA hydrogel with a layer thickness of 240μm at different temperatures. The inset is the solar irradiance spectrum (grey area). (B) The luminous (T_{lum}), IR (T_{IR}) and solar (T_{solar}) transmittances (solid line) and corresponding transmittance modulations (ΔT_{lum}, ΔT_{IR}, and ΔT_{solar}) (dash line) in response to the temperature.

Figure 5 Solar-energy shielding performance of the pNIPAm-AEMA device. (A) Temperature profiles of a thermometer inside the model chamber affixed with double glass slides (red) or a pNIPAm-AEMA device as the window. (B_1 – B_2) Visible images and corresponding thermal infrared images of a 2″ × 2″ pNIPAm-AEMA device before and after phase transition. (B_3) IR images of a pNIPAm-AEMA device under illumination of a NIR source (850 – 2000nm) captured by an IR camera. (C) The solar transmittance (T_{solar}) and (D) transmittance modulations (ΔT_{lum}, ΔT_{IR}, and ΔT_{solar}) of the pNIPAm-AEMA device (380μm layer thickness) measured after every 100 heating-cooling cycles.

Supplemental information

Supplemental Information includes Supplemental Figures, Experimental Procedures, and Simulations, and Supplemental video (1000 heating-cooling cycle test) can be found with this article online at .....

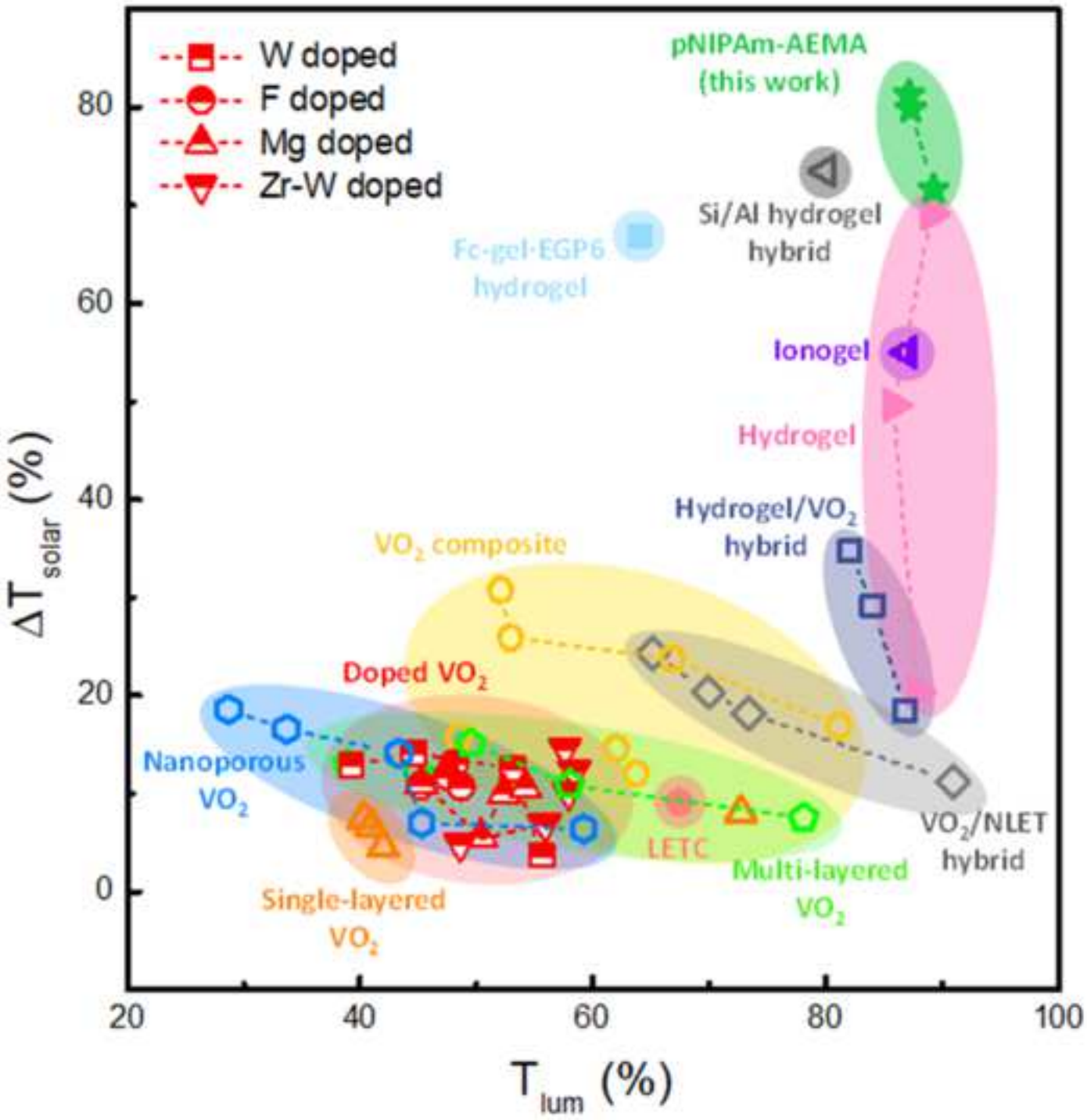

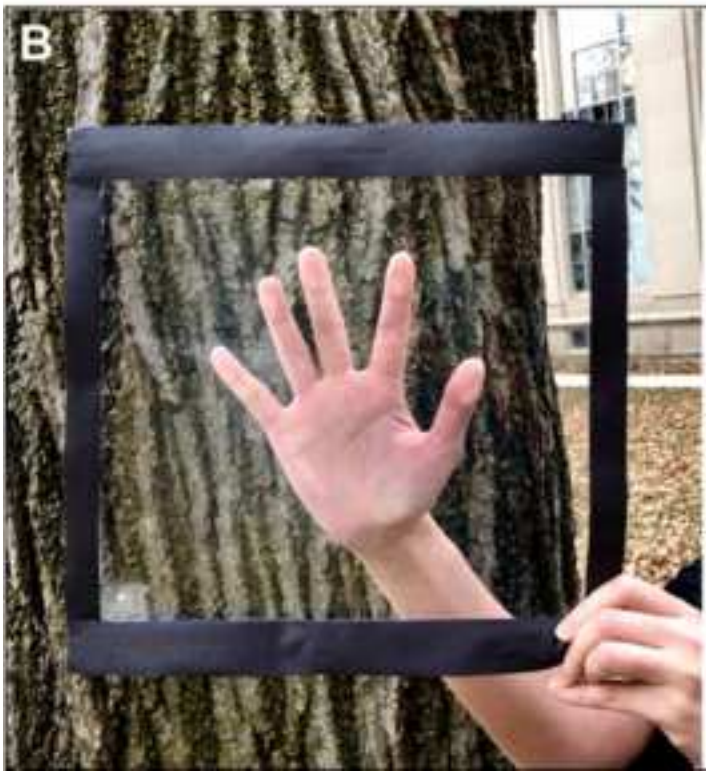

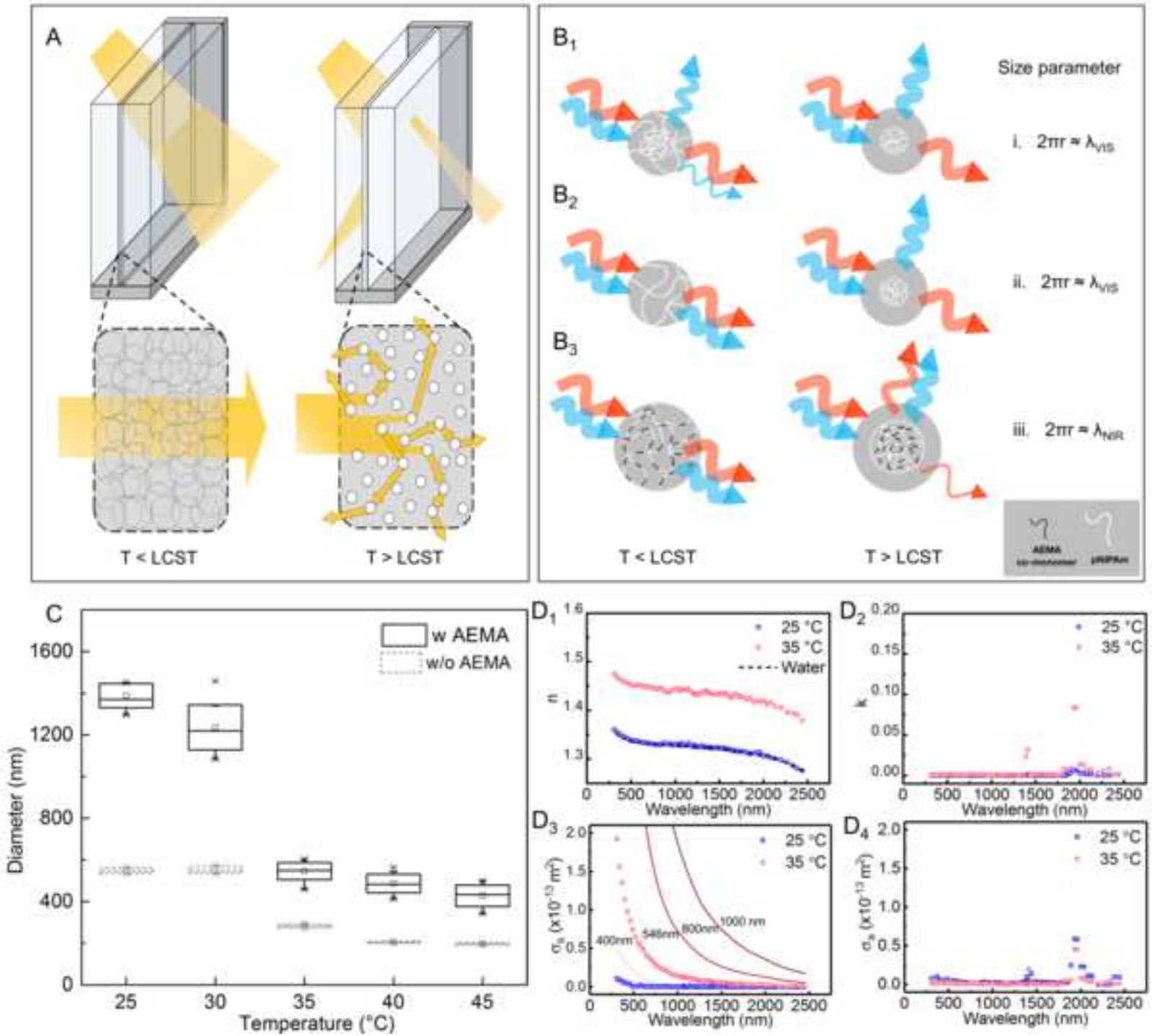

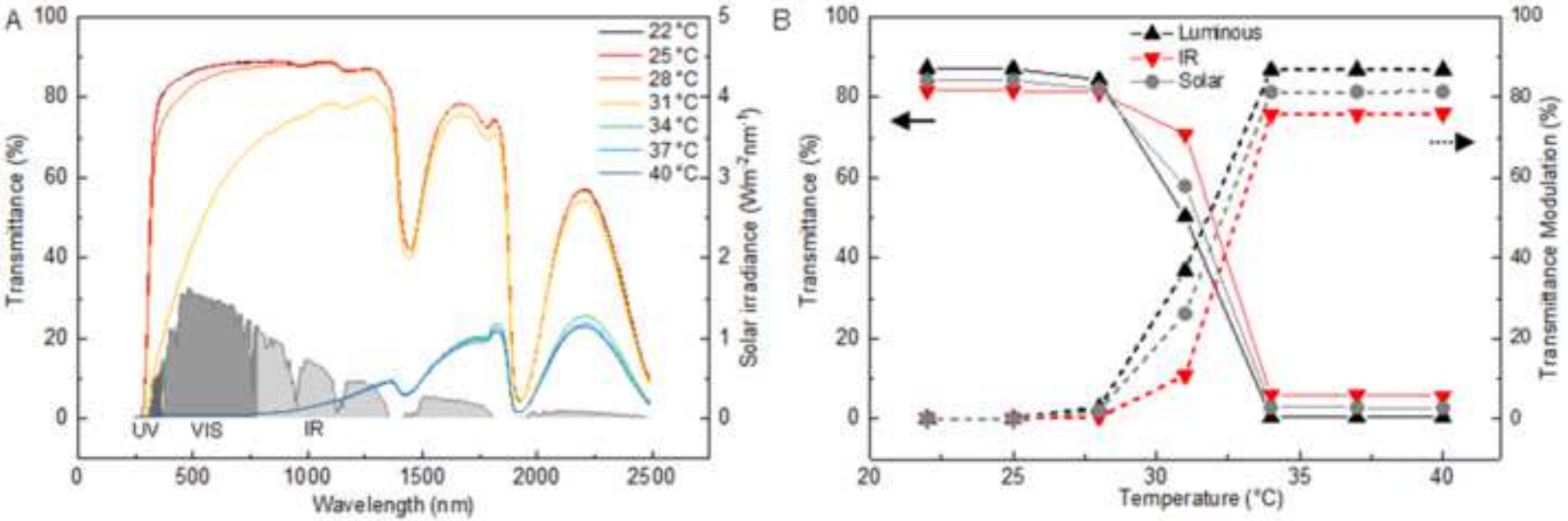

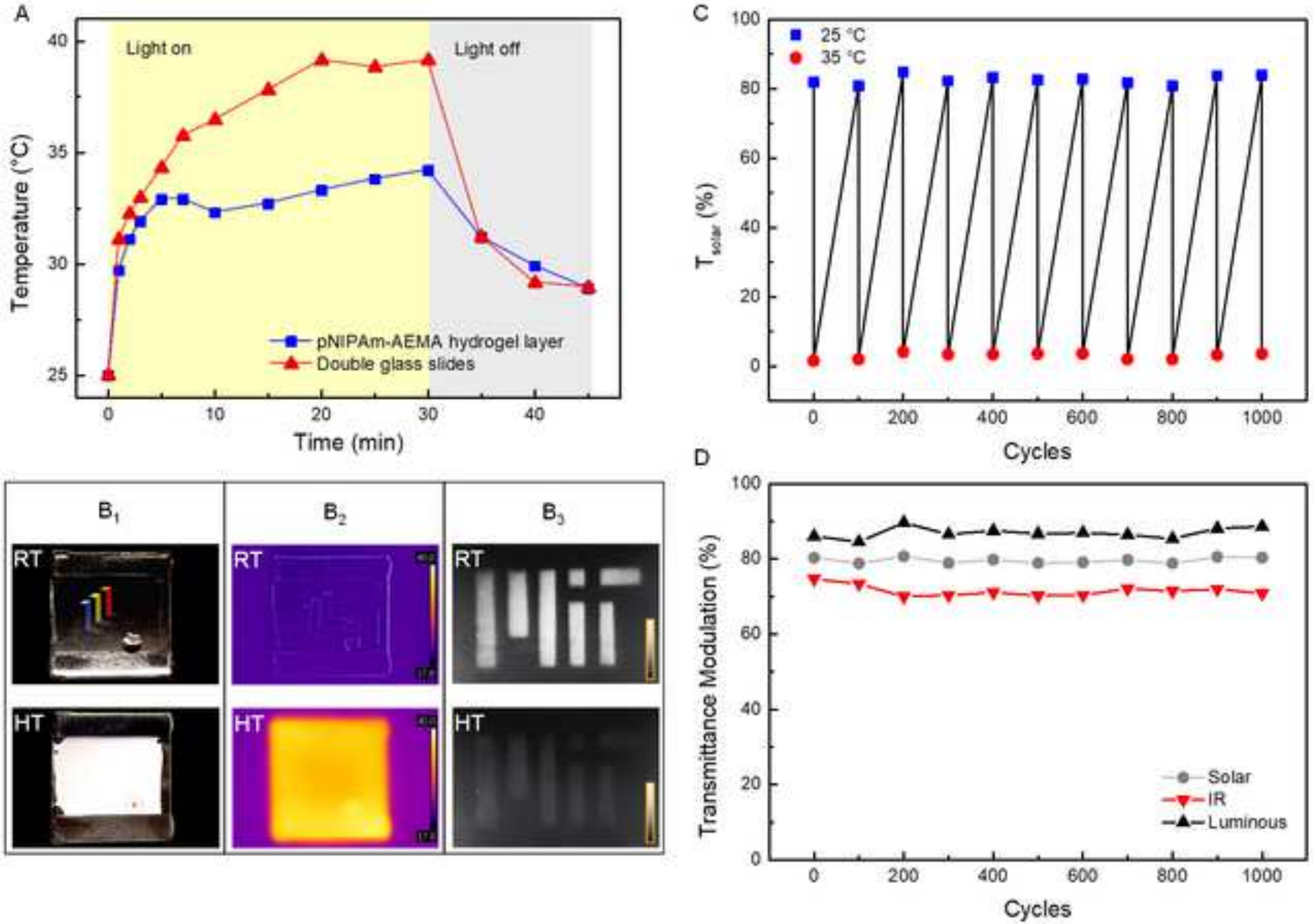

Supplemental Figures

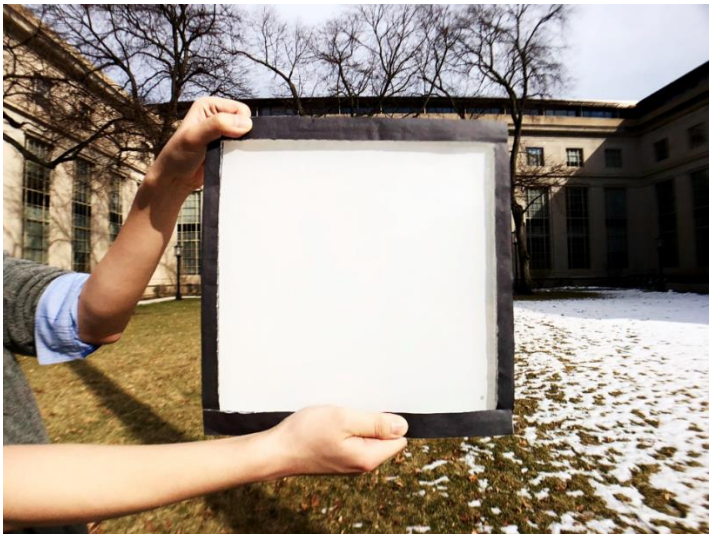

Figure S1 Image of a 12″ ×12″ pNIPAm-AEMA device after phase transition.

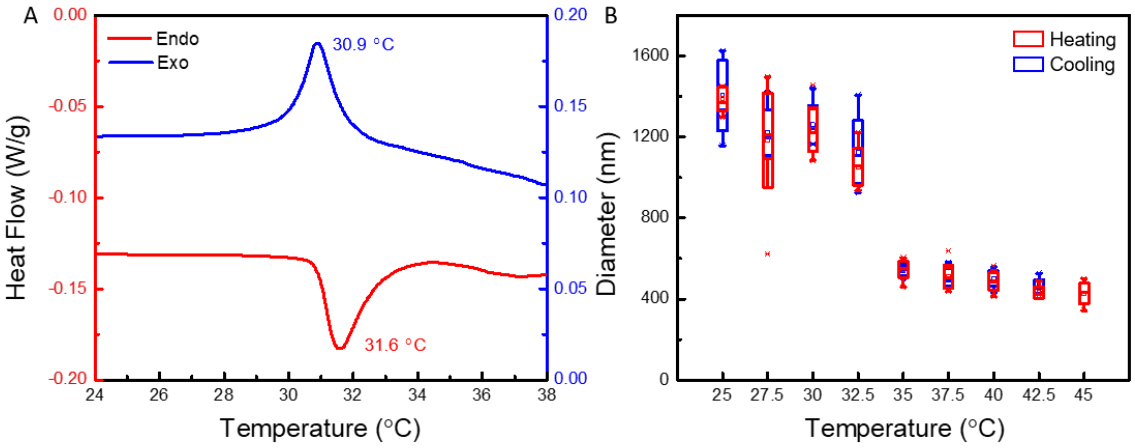

Figure S2 Characterization of the LCST of pNIPAm-AEMA microparticles. (A) DSC measurement of normalized heat flow in the endothermic (Endo) and exothermic (Exo) process. (B) Temperature dependence of the hydrodynamic diameter of pNIPAm-AEMA microparticles in heating and cooling operations measured by DLS.

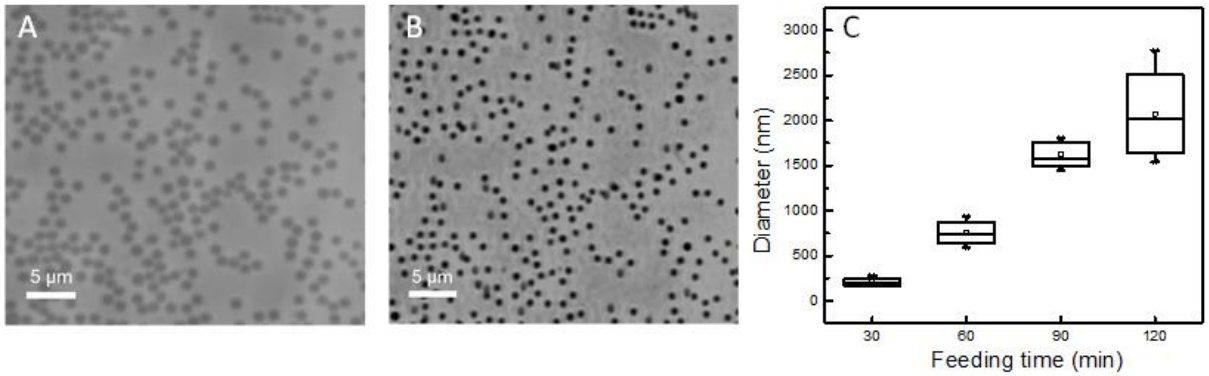

Figure S3 Micro-sized pNIPAm-AEMA particles. (A and B) Optical microscope images of the pNIPAm-AEMA microparticles synthesized by continuous feeding for 75min. (A) Before phase transition, D_h is 1388nm at 25˚C. Scale bar is 5 μm. (B) After phase transition, D_h reduces to546nm at 35˚C. Scale bar is 5 μm. (C) Hydrodynamic diameter of the co-polymerized pNIPAm-AEMA particles at 25˚C. To keep a constant co-monomer concentration for injection, the pNIPAm-AEMA particles grow linearly in dimension with the increasing of feeding time.

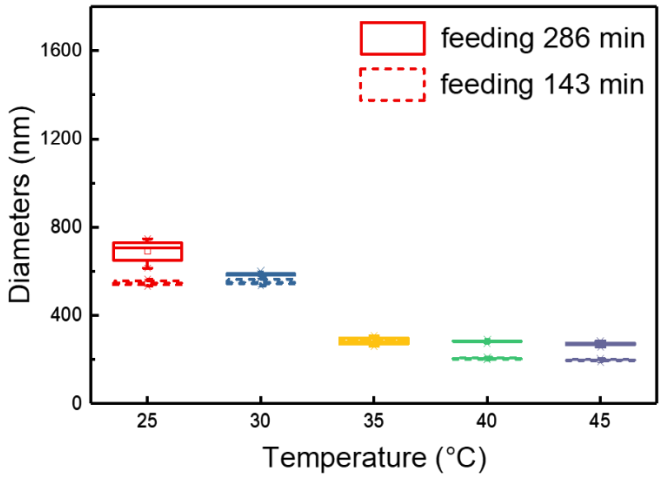

Figure S4 Size limitation of pNIPAm particles synthesized by continuous feeding method. Hydrodynamic diameters of pNIPAm particles synthesized by continuous feeding for 143min (dash box) and 286min (solid box) as a function of temperature. To carry out the polymerization for a longer time and a larger amount of monomers (100% increment). There is only 26% increase of D_h at 25˚C and 1.3% increase at 35˚C.

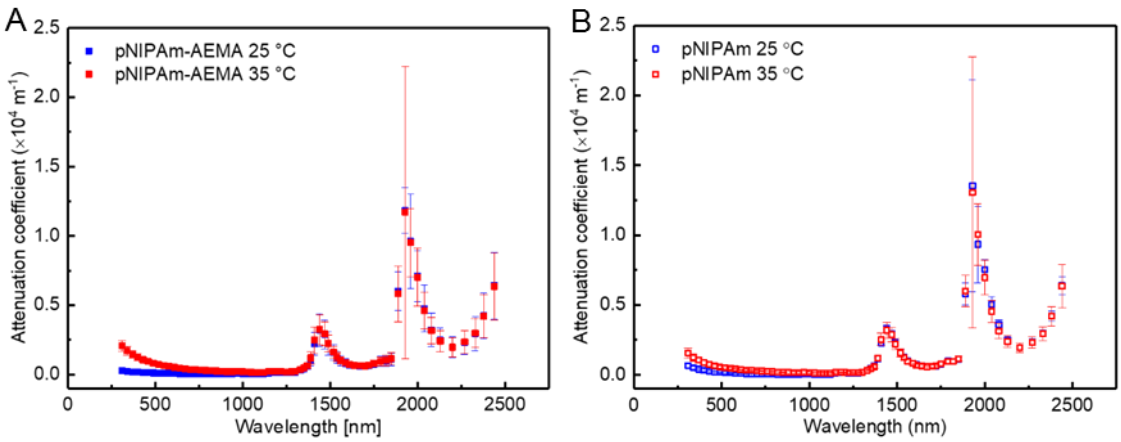

Figure S5 Attenuation coefficient of hydrogel particle suspension. (A) The attenuation coefficient of the pNIPAm-AEMA microparticle suspension, obtained from suspension with thicknesses of 130μm, 320μm, 470μm and 620μm. (B) The attenuation coefficient of the pNIPAm particle suspension, obtained from suspension with thicknesses of 130μm, 300μm, 460μm and 670μm. Error bars represent the 95% confidence intervals of fitted attenuation coefficients. Two peaks near 1450nm and 1930nm are associated with the strong absorption of water molecules.[1]

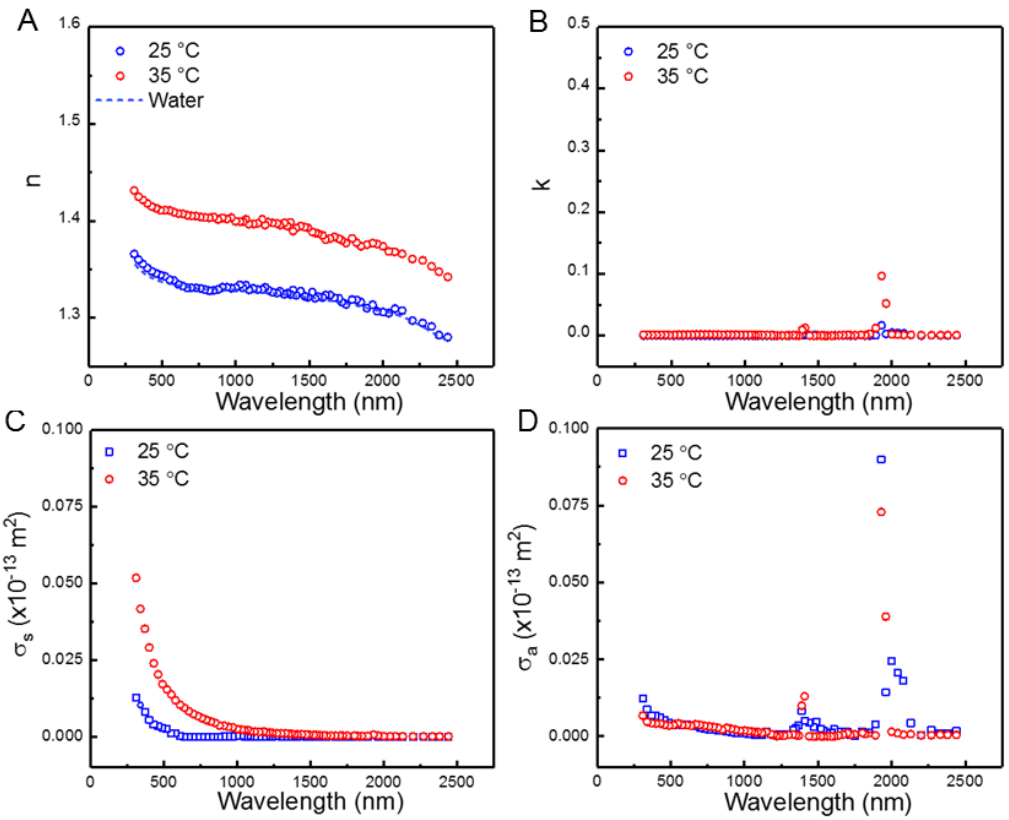

Figure S6 Optical properties of pNIPAm hydrogel particles. (A, B) Real (*n*) and imaginary (*k*) part of refractive index of the pNIPAm hydrogel particles at 25°C and 35°C, obtained through the inverse method. The dashed line in (A) shows the *n* of water. (C, D) Corresponding scattering and absorbing cross-sections of the hydrogel particles at 25°C and 35°C.

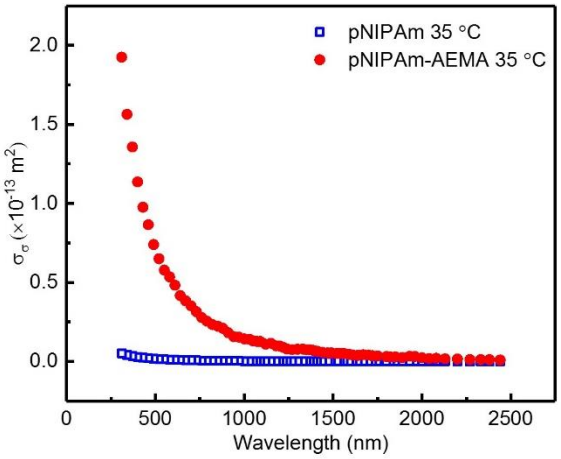

Figure S7 Comparison of scattering cross-sections between pNIPAm particles and pNIPAm-AEMA microparticles at 35°C.

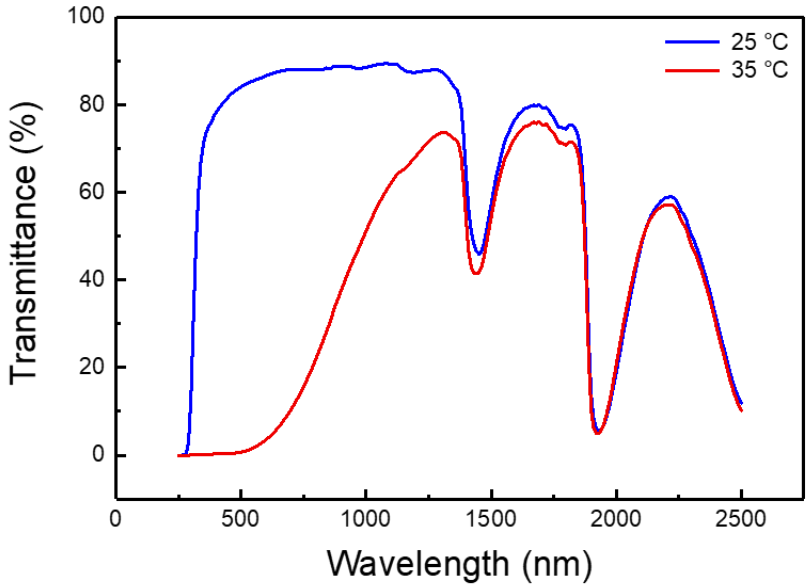

Figure S8 Transmittance spectra of the pNIPAm particles with a layer thickness of 240µm before (25˚C) and after phase transition (35˚C).

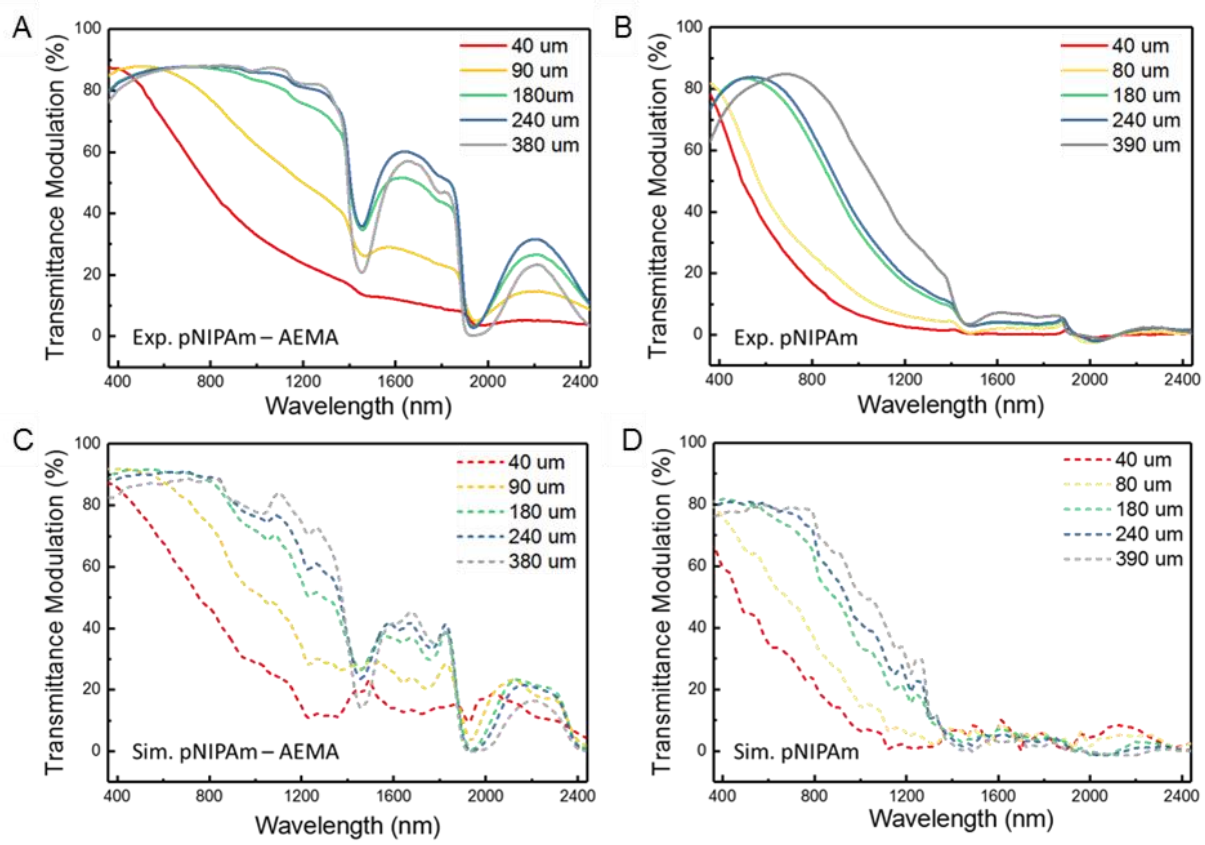

Figure S9 Transmittance modulation by pNIPAm-AEMA and pNIPAm hydrogel with different layer thicknesses. Experimental (A and B) and the Monte-Carlo simulation (C and D) results of transmittance modulation ($T_{25°C} - T_{35°C}$) by pNIPAm-AEMA microparticles with the layer thickness from 40 to 380μm, and pNIPAm particles with the layer thickness from 40 to 390μm. Large absorption of UV light by the double glass slides at the wavelength range below 360nm causes the deviation between experiments and simulations, which is excluded in the figure. This deviation is negligible for the estimation of the solar modulation due to the small portion of solar irradiance in the UV region.

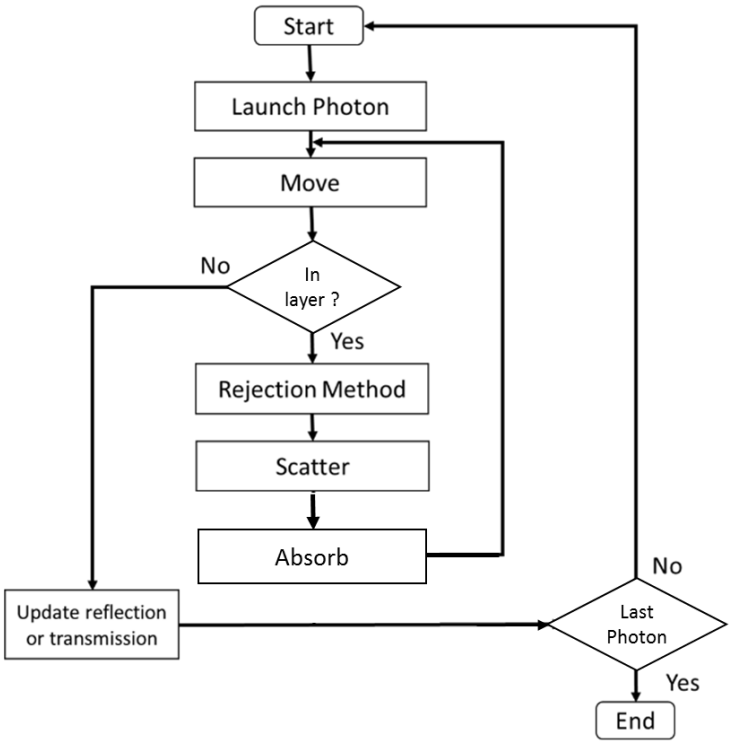

Figure S10 Logic flow of the Monte-Carlo simulation.

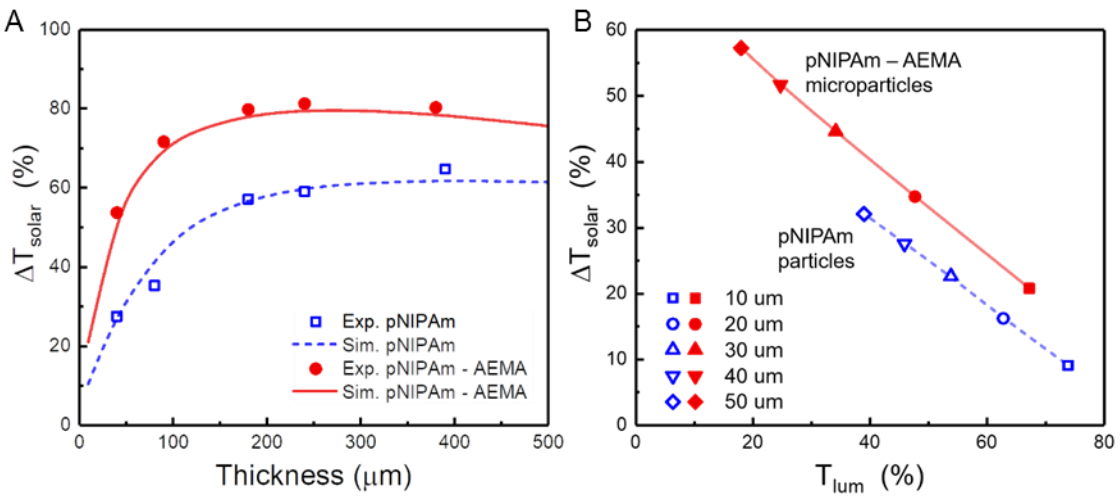

Figure S11 Thickness-dependent thermochromic properties of pNIPAm-AEMA and pNIPAm hydrogel. (A) Dependence of ΔT_{solar} on the layer thickness of the pNIPAm-AEMA and the pNIPAm hydrogel, obtained from the experiment and the Monte-Carlo simulation. (B) ΔT_{solar} and T_{lum} at 35°C (after phase transition) of the pNIPAm-AEMA hydrogel and the pNIPAm hydrogel with the layer thickness from 10 to 50μm, obtained from the Monte-Carlo simulation.

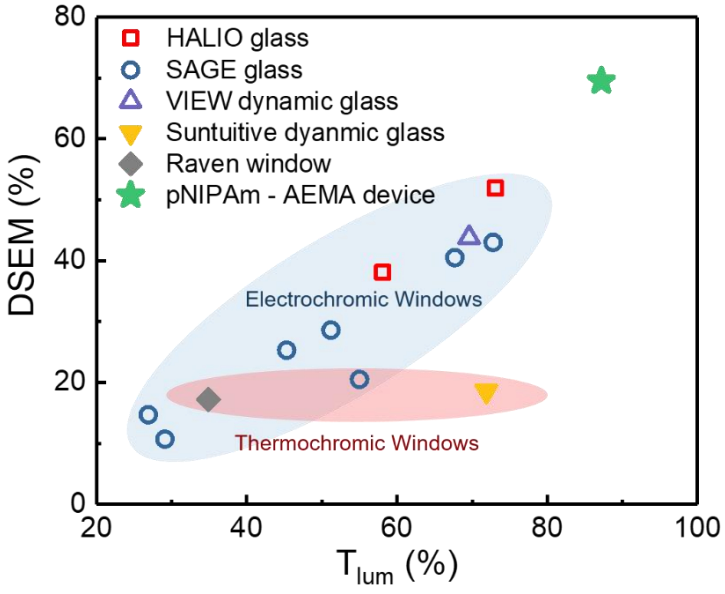

Figure S12 Comparison of direct solar-energy modulation (DSEM) and luminous transmittance (T_{lum}) between the pNIPAm-AEMA device with available smart dynamic windows on the market.[2] Solid symbols represent thermochromic windows, while hollow symbols represent electrochromic windows.

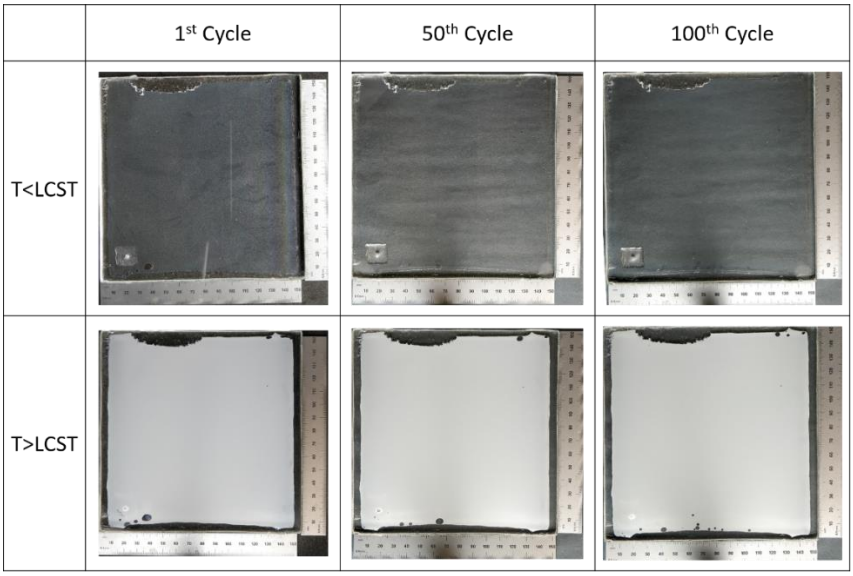

Figure S13 Visible Images of a 6" × 6" pNIPAm-AEMA device before and after phase transition captioned during 1st, 50th and 100th heating-cooling cycle.

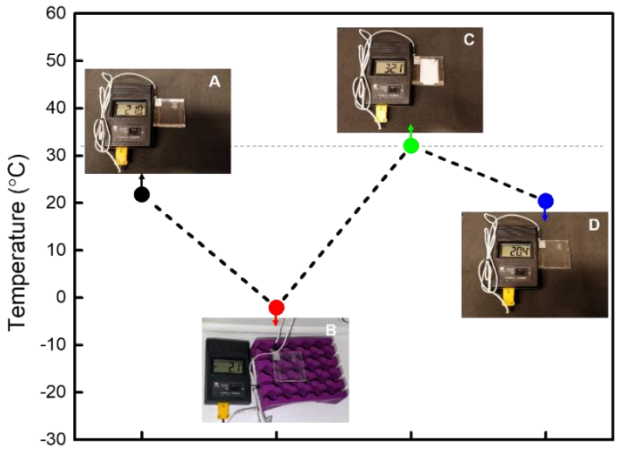

Figure S14 Optical images of a pNIPAm-AEMA device at temperature of (A) 21.8°C, (B) −2.1°C (freezing at −4°C for 5 min), (C) 32.1°C, and (D) 20.4°C.

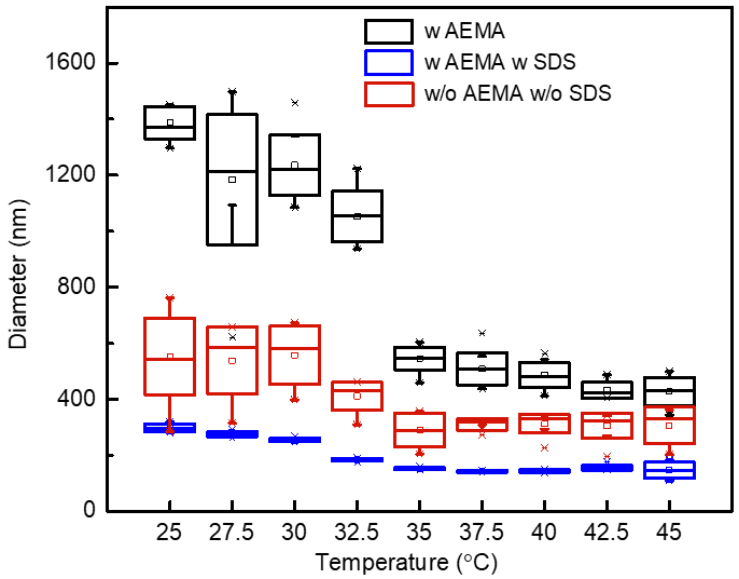

Figure S15 Effects of AEMA and SDS on the synthesis of microparticles. Hydrodynamic diameters of pNIPAm-AEMA (black; 1388nm at 25°C; 546nm at 35°C), pNIPAm-AEMA with SDS (blue; 298 nm at 25 °C; 193 nm at 35 °C, SDS was added during the continuous feeding polymerization), and pNIPAm (red; 555 nm at 25 °C; 287 nm at 35 °C) hydrogel particles. The three different batches were synthesized using the same method as mentioned in the experimental section. Adding AEMA co-monomer is responsible for the increase of particle size while adding SDS surfactant during polymerization reduces particle size and avoids aggregation.[3]

Supplemental Experimental and Simulation Procedures

Supplemental Note 1: Simulation of multiple scattering in thin hydrogel layer

The thickness-dependent ΔT_{solar} of the hydrogel smart window devices was investigated by experiments and a modified Monte-Carlo simulation.[4] ΔT_{solar} of the devices with the layer thickness ranging from 40 to 390μm were measured. In the simulation, the effect of randomly distributed hydrogel particles on the propagation of light is modeled as multiple scattering and absorbing events. The logic flow of the modified Monte-Carlo simulation is provided in Figure S10.

A single photon was launched at the upper boundary of the hydrogel layer in each run, with a normal propagation direction to the surface. Then the photon moves until it is reflected by or transmits through the hydrogel layer. For each moving step, the photon travels a random distance of ΔS, whose mean value is the same as the mean free path of the photon in this medium:[4]

$$\Delta S = -\frac{\ln(\zeta)}{\mu_s + \mu_a} \tag{S.1}$$

where ζ is a pseudo random number locates in (0,1]. $1/(\mu_s+\mu_a)$ is the mean free path of photons in the hydrogel layer. The concentration of the close-packed hydrogel particles after centrifuging was estimated as $6/(\pi D_h^3)$. The scattering and absorbing cross-sections of pNIPAm-AEMA microparticles (Figure $3D_3$ and $3D_4$) and pNIPAm particles (Figure S5C and S5D) estimated through the inverse method were applied to determine the μ_s and μ_a.

The photon changes the propagation direction after each moving step as the scattering occurs. The new propagation direction is determined by a rejection method following the phase function $P(\theta)$ of Mie theory, where θ denotes the scattering angle.[4] Basically, two pseudo random numbers are generated, which are the random scattering phase function (P_{rand}) and the random scattering angle (θ_{racd}). The random scattering angle is accepted as the propagation direction for the next moving step if $P_{rand} \leqslant P(\theta_{racd})$. Otherwise, new P_{rand} and θ_{racd} will be generated until the new propagation direction is determined. The light absorption by water inside and outside the hydrogel particles is modeled with a weight function W applied on the photon[4], where the original weight W_0 before launching is 1. To avoid the inaccuracy near the wavelength of 1450nm and 1930nm, the weight attenuation after n^{th} moving step is accounted as,

$$W_n = W_{n-1} \exp(-\frac{4\pi k_w}{\lambda} \Delta S_n) \tag{S.2}$$

where ΔS_n is the n^{th} moving distance. The moving steps repeat until the photon travels out of the upper or lower boundary of the hydrogel layer with a specific weight.

Reflectivity (R) of normal incidence at the boundary of two materials with the reflective index of n_1 and n_2 is

$$R = \left[\frac{n_2 - n_1}{n_2 + n_1}\right]^2 \tag{S.3}$$

n_{glass} = 1.5, n_{water} = 1.33 and n_{air} = 1.0 were used to estimate the reflectivity at the boundaries between glass and air (R_{ga}) and the boundaries between the glass and the hydrogel layer (R_{gh}). A total transmittance of 92% was obtained, where the multiple reflections between boundaries are negligible.

$$T = (1-R_{ga})^2 \cdot (1-R_{gh})^2 \approx 92\% \quad \text{(S.4)}$$

5×10^3 photons were simulated for each wavelength to obtain the ΔT_{solar} with fluctuations less than 0.5%.

Transmittance modulation of pNIPAm-AEMA and pNIPAm hydrogel with different layer thicknesses measured with UV-Vis-NIR spectrometer (Lambda 1050, PerkinElmer, USA) are shown in Figure S9A and S9B, which were well reproduced by the Monte-Carlo simulation, as shown in Figure S9C and S9D. The dependence of ΔT_{solar} on the layer thickness for pNIPAm-AEMA and pNIPAm hydrogel were shown in Figure S11A. The ΔT_{solar} of the pNIPAm-AEMA hydrogel raised with the increasing of the layer thickness, which is apparently higher than that of the pNIPAm due to the extending of scattering into the IR region. The maximum ΔT_{solar} of 81.3% was attained at 240μm for the pNIPAm–AEMA, while the pNIPAm achieved the maximum ΔT_{solar} of 64.8% at 390μm. Further increase of thickness caused a reduction in ΔT_{solar} since the transmittance in the visible region is decreased, and the water absorption in the IR range is saturated before the phase transition.

A high T_{lum} of the thermochromic layer after phase transition is required in some situations.[5] The thickness of the hydrogel layer needs to be reduced to improve the T_{lum} at high temperatures. Figure S11B shows the Monte-Carlo simulation results of the ΔT_{solar} and T_{lum} at 35˚C for devices with the layer thickness from 10 to 50μm. At the same T_{lum}, the ΔT_{solar} of the pNIPAm-AEMA hydrogel is higher than that of the pNIPAm hydrogel due to the full solar spectrum modulation. Besides, the layer thickness of the pNIPAm-AEMA hydrogel to achieve a specific ΔT_{solar} is smaller than that for the pNIPAm hydrogel. This simulation shows the potential of the pNIPAm pNIPAm-AEMA hydrogel to achieve a high T_{lum} of 50% after phase transition and a decent ΔT_{solar} of 30% by decreasing the layer thickness to 20μm, which requires precise packaging method and is beyond the scope of this work.

Supplemental Note 2: Direct Solar-Energy Modulation (DSEM)

The direct solar-energy modulation (DSEM) was introduced to identify the solar-energy shielding ability in this work, which is the magnitude change of the total solar irradiance (mW/cm^{-2}) passing through the window device before and after phase transition. Experimentally, the intensity of a solar simulator was calibrated to $100mWcm^{-2}$ (one sun) on a crystalline silicon standard solar cell, upon which the pNIPAm-AEMA hydrogel device was installed afterward. A total acquisition of solar irradiance passing through the window device was guaranteed by this configuration.

Supplemental Note 3: Synthesis of pNIPAm particles

213ml DI water was heated to 80˚C and purged with N_2 during the entire reaction. Before the polymerization, two monomer solutions were prepared separately and degassed by vacuum at the room temperature. The first batch of monomer solution consisted of 0.33g NIPAm and 6.69mg BIS in 13.7ml DI water and injected into the reaction vessel directly; while the second batch of monomer solution was prepared in 21.75ml DI water with 3.36g NIPAm and 168mg BIS, which was transferred into a syringe. 0.76ml of 0.19M SDS was also injected into the reaction vessel and stirred at 1000rpm. Whereafter, the polymerization was initiated by adding 0.76ml of 0.36M APS solution. After one minute, the second batch of monomer solution was fed into the reaction vessel by a syringe pump at the rate of 200μl/min. The reaction was stopped after all monomers were fed and the suspension was quenched in the same way as for pNIPAm-AEMA microparticles.

Supplemental References

1 Ma, X., Lu, J. Q., Brock, R. S., Jacobs, K. M., Yang, P. & Hu, X.H. (2003) Determination of complex refractive index of polystyrene microspheres from 370 to 1610 nm. Physics in medicine and biology *48*, 4165.

2 Lawrence Berkeley National Laboratory, International Glazing Database, version 60 https://windows.lbl.gov/software/igdb. (accessed June 2018).

3 McPhee, W., Tam, K. C. & Pelton, R. (1993) Poly (N-isopropylacrylamide) latices prepared with sodium dodecyl sulfate. J. Colloid Interf. Sci *156*, 24-30.

4 Ramella-Roman, J. C., Prahl, S. A. & Jacques, S. L. (2005) Three Monte Carlo programs of polarized light transport into scattering media: part I. Opt. Express *13*, 4420-4438.

5 Zhou, Y., Cai, Y., Hu, X. & Long, Y. (2014) Temperature-responsive hydrogel with ultra-large solar modulation and high luminous transmission for "smart window" applications. J. Mater. Chem. A *2*, 13550-13555.